Electromagnetically induced transparency in an open V-type molecular system

A. Lazoudis, T. Kirova, E. H. Ahmed, P. Qi, J. Huennekens, and A. M. Lyyra

Phys. Rev. A **83**, 063419 — Published 27 June 2011

DOI: 10.1103/PhysRevA.83.063419

ELECTROMAGNETICALLY INDUCED TRANSPARENCY IN AN OPEN V-TYPE MOLECULAR SYSTEM

A. Lazoudis[1,a], T. Kirova[2], E. H. Ahmed[1], P. Qi[1,b], J. Huennekens[3], and A. M. Lyyra[1,c]

1. Department of Physics, Temple University, Philadelphia, Pennsylvania 19122-6082
2. NITeP, Wallenberg Research Centre, 10 Marais Street, Stellenbosch 7600
South Africa
3. Department of Physics, 16 Memorial Drive East, Lehigh University, Bethlehem, Pennsylvania
18015

Abstract

We report experimental observation of electromagnetically induced transparency (EIT) in an inhomogeneously broadened V-type Na_2 molecular system. The experiment is performed with both co- and counter-propagating arrangements for the propagation direction of the coupling and probe laser beams. In our theoretical model we employ the density matrix formalism, as well as perturbative methods for obtaining the probe field absorption profile for both open and closed systems. Simulations of the experimental data show excellent agreement with the predictions derived from the basic theory. Our fluorescent intensity measurements show that in the co-propagating configuration the EIT plus saturation window depth is about 95%, while under similar conditions in the counter-propagating geometry we observed 40-45% reduction in the fluorescence signal around line center. To separate the two simultaneously occurring mechanisms in a V-type system, namely EIT and saturation, that are induced by the coupling field, we have carried out theoretical calculations, which show that in the co-propagating case a significant fraction of the depth of the dip is due to the coherent effect of EIT. When the coupling and probe beams are in counter-propagating configuration, the dip is mostly due to saturation effects alone.

PACS numbers: 33.40.+f, 42.50.Ct, 42.50.Gy

[a] current address: Research & Development Department, Ellinogermaniki Agogi, Dimitriou Panagea Str., 15351 Pallini, Greece

[b] current address: Department of Radiation Oncology, Cleveland Clinic, 9500 Euclid Avenue, Cleveland OH 44195

[c] corresponding author

1. Introduction

The goal of achieving electromagnetically induced transparency (EIT) through coherence effects has led to a great deal of experimental and theoretical interest in various three level atomic system configurations [1-5]. Since its first demonstration, which was based on a Λ-type energy level system [6], EIT has been observed in several experiments that were performed on V-type atomic systems [7]. In the so-called V configuration (see Figure 1), the two upper excited states are coupled to a single lower ground state. Indicating how EIT occurs via quantum interference in a V-type system is of special interest because no population trapping is involved. Thus, such a system can be used to highlight the distinction between various coherent processes such as EIT and coherent population trapping [8].

The V-type excitation scheme differs from the Λ-type EIT in that two separate effects occur simultaneously, EIT and saturation, with very different nature. Unlike the Λ-type excitation scheme, in the V-type scheme the stronger coupling laser shares the initial (lower) level with the weak probe laser and causes a depletion of the initial state population (i.e., saturation) to occur. Thus both EIT and saturation are observed simultaneously in the experiment, and the experimental signatures of these two physically distinct effects are hard to disentangle. In order to actually separate the relative contributions, it is necessary to treat the co- and counter-propagating laser geometries both experimentally and through a rigorous theoretical modeling. In order to distinguish the contributions from these two separate mechanisms full density matrix calculations need to be applied.

Although extensively studied in atoms, investigations of EIT phenomena in molecules are still scarce. Recently EIT has been demonstrated experimentally in Doppler-broadened Li_2 [9, 10], K_2 [11], and Na_2 gases [12], acetylene molecules in a hollow-core photonic gap-fiber [13, 14], acetylene photonic microcell [15] and in Cs_2 in a vapor cell [16].

Unlike atoms, molecules constitute open systems in that the upper states have more than one decay channel available to lower energy levels that are not involved in creating the coherent effect. In addition, molecular transition dipole moment matrix elements [17-21] are much smaller than in atoms, making the use of commercial, average power, continuous wave (cw) lasers for molecular excitation schemes non-trivial.

Recently a V-type molecular EIT study has been performed in acetylene [15] and shows that the use of counter-propagating beams, which is in general considered unfavorable for the V-type excitation due to a larger residual Doppler width, can be used as a new spectroscopic technique for velocity discrimination. The residual Doppler width for the V- and Λ-type excitation schemes is $\Delta\nu_D = \left|\vec{k}_1 - \vec{k}_2\right|\upsilon_{\mathrm{p}}$, where υ_{p} is the most probable molecular velocity and k_1 and k_2 are the wavenumbers of the probe and coupling lasers. The less pronounced EIT feature in the case of the unfavorable beam propagation direction is explained with the varying Autler-Townes (AT) splitting [22] for each velocity group which leads to the absorption of one velocity group encroaching on the transparency of the other. The basis of this effect is theoretically outlined in the work of Shepherd *et al*. [23] in which the wavelength and propagation direction dependence of EIT in Doppler-broadened media was studied. The authors validate their theoretical results on the wavelength effects by carrying out an EIT experiment in Rb vapor.

The purpose of the current work is to report an experimental observation of EIT in an inhomogeneously broadened V-type molecular system with two different beam geometries with the specific goal of observing and modeling the two distinct and different physical effects, EIT and saturation. The medium chosen to interact with the two applied laser fields is a thermal sodium vapor and the experimental arrangement uses co- or counter-propagating coupling and probe beams. We start with a description of the selected energy level excitation scheme and the experimental apparatus, followed by a presentation of the recorded fluorescence intensity measurements (Section II). To understand the modification of the transparency induced by the strong coupling field in the system introduced above, we utilize the density matrix formalism which is presented in Section III a). An alternative theoretical analysis, based on perturbation theory, which describes a steady-state investigation of an open molecular system, is carried out in Section III b). Inclusion of the Doppler effect and description of the observed fluorescence signal is described in Section III c). Section IV describes simulation of the experimental signals including saturation effects and provides a link between the experimental data and the predictions derived from the basic theory. In addition, we discuss the physical constraints and parameters that lead to the reduction or extinction of EIT in Doppler broadened systems of various beam geometries. Our conclusions are given in Section V.

II. Experimental Setup and Excitation Scheme

The level diagram and experimental setup used in the exploration of EIT in diatomic molecules with a V-type energy configuration are shown in Figures 1, and 2, respectively. The experimental setup is similar to the one previously described in [9, 17].

Sodium dimer molecules were generated in a five arm heat-pipe oven [24] heated to a temperature of 650 K. The temperature was determined by the Doppler linewidth of a single laser excitation. In order to prevent deposition of metal on the windows of the heat-pipe oven, argon was used as a buffer gas. The pressure of the argon gas was kept as low as possible (260-320 mTorr, measured at room temperature), since high buffer gas pressures can lead to excessive collisional broadening that could mask the coherent effects. The vapor pressure at 650 K is 194.8 mTorr for Na and 3.514 mTorr for Na_2 [25].

The optical fields in both experiments were produced by two cw Coherent 699-29 ring dye lasers. Each tunable dye laser was pumped separately by a current stabilized argon ion laser and generated single mode output at a wavelength corresponding to the selected probe or coupling transition. The two laser beams were linearly polarized in the vertical direction and were overlapped in the center of the heat-pipe. The probe field (weak laser) was modulated by an optical chopper connected to the lock-in amplifier. The chopper was used to periodically vary the field with time and thus allow use of phase sensitive detection. The chopping frequency was 1.04 kHz.

Within our selected energy level system (see Figure 1) two variations in the geometry of the propagation direction of the laser beams were investigated in order to gain insight into the role of the residual Doppler line widths on the EIT behavior of the system. In the first experimental arrangement, the two laser beams were combined in a co-propagating geometry while in the second experimental setup the laser beams were arranged to propagate in opposite directions. Since the only difference between the two sets of experiments lies in the geometry of the applied laser fields, the descriptions of the interaction medium, the detection methods, and the apparatus employed are the same in both experimental arrangements.

The modulated fluorescence emitted by molecules in the excited state, as a result of the probe laser excitation, was directed through a set of highly reflective mirrors from the side window of the heat-pipe into a double monochromator (SPEX 1404) with a cooled photomultiplier (PMT). The monochromator was set to a preferred spontaneous emission wavelength for single rovibronic fluorescence (single-channel) detection while the signal of the PMT was fed to a lock-in amplifier (SR850 DSP) with a 300 ms time constant. As the probe laser was scanned through the desired transition, the lock-in output was recorded by the computer controlling the laser scan as a function of laser frequency.

To ensure that all the molecules probed by the weak field were exposed to the strong field in the region of least electric field variation, the focal spot size of the coupling laser beam was adjusted to be significantly greater than the spot size of the probe laser beam. Hence, the coupling field was focused to a minimum diameter of 986 μm and 720 μm (at $1/e^2$ intensity of the Gaussian spatial profile) for the counter-propagating and co-propagating cases, respectively, while the probe laser spot size diameter was set to 210 μm in both cases.

The V-type energy level structure of the Na_2 dimer used for this study is schematically depicted in Figure 1. The experiment was carried out using optical transitions between the ground state [26, 27] level $X^1\Sigma_g^+$ (v″=0, J″=14) and two excited levels [28], $A^1\Sigma_u^+$ (v′=6, J′= 13) and $A^1\Sigma_u^+$ (v′=7, J′=13). In our V-type system the ground state level $X^1\Sigma_g^+$ (v″=0, J″=14) serves as a common state for the probe and coupling transitions. A single-photon excitation is induced by the probe laser driving the $X^1\Sigma_g^+$ (v″=0, J″=14) → $A^1\Sigma_u^+$ (v′=7, J′=13) transition, as sketched in Figure 1. In addition, a second laser field is coupled to the $X^1\Sigma_g^+$ (v″=0, J″=14) → $A^1\Sigma_u^+$ (v′=6, J′=13) transition. In Figure 1, we label the ground state level $X^1\Sigma_g^+$ (v″=0, J″=14) as level |2>, and the excited state levels $A^1\Sigma_u^+$ (v′=6, J′=13) and $A^1\Sigma_u^+$ (v′=7, J′=13) as |3> and |1>, respectively. EIT and saturation effects can be observed as a dip in either the probe field absorption profile, or in the fluorescence signal of the intermediate level, as shown in [2, 29] for the case of a cascade type excitation scheme. In our experimental set-up we choose to observe the EIT effect through fluorescence rather than absorption. We monitor the population of the upper state level $A^1\Sigma_u^+$ (v′=7, J′=13) via single-channel fluorescence detection while scanning the frequency of the probe field around the |2>→|1> transition and keeping the strong coupling field on resonance with the |2>→|3> transition. For this purpose, the double monochromator was set at a wavelength of 681.4 nm corresponding to the molecular decay from the upper level $A^1\Sigma_u^+$ (v′=7, J′=13) to the ground state level $X^1\Sigma_g^+$ (v″=5, J″=12) (level |4′> in Figure 1).

In the absence of the coupling field, monitoring the fluorescence of the |1>→|4′> transition for the probe field scan yields the usual Doppler-broadened fluorescence spectrum (see Figure 3a) with line width of 1.23GHz. When both laser fields travel simultaneously through the Doppler-broadened vapor, the relative direction of their propagation becomes critical to the observation of coherence effects, at lower coupling field intensity. Our recent theoretical [30] analysis of the role of Doppler broadening on AT splitting in molecular cascade excitation schemes shows that the splitting strongly depends both on the propagation direction and the wavenumber ratio of the coupling and probe laser fields. The latter was confirmed experimentally in our study of the AT effect in sodium dimer vapor [12], in which the optimal conditions for its observation under different wavenumber ratio scenarios was investigated. Hence, here we experimentally investigate the influence of the propagation directions of the probe and coupling fields on the absorption of the weak probe field.

In a V-type system, as will be discussed later in detail, co-propagating beams act to reduce the residual Doppler line width. Furthermore, since the reduction depends on the wavelength mismatch, in this geometry the effect of molecular motion can be eliminated if the optical fields have similar wavelengths. Under the action of both fields, in the limit of a weak probe and a strong coupling laser, we monitor the population of the upper state level $A^1\Sigma_u^+$ (v′=7, J′=13) and observe a sharp dip in the center of the fluorescence spectrum (Figure 3b). This dip corresponds to the interaction with the strong coupling field and the depth of the dip is an indication of both EIT and saturation effects, which contribute simultaneously. It can be seen that in this configuration the window depth is about 95%. (Figure 3c) shows the recorded fluorescence from level |1> for a coupling field turned slightly off resonance. The power of the coupling laser throughout the experiment was 265-270 mW while the probe beam was attenuated to less than 1 mW.

In the counter-propagating geometry, despite the fact that the beams were arranged so as to maximize the residual Doppler line width (see section IIIc), we were able to observe a 40-45% reduction in the fluorescence signal around the line center (Figure 4). However, in this case, the dip is dominated by saturation effects as will be shown below in our analysis.

III. Theory

a) Density Matrix Formalism in an Open Three-Level Vee System

A physical understanding of the behavior of an open V-type system in the weak probe field regime can be achieved by adopting the density matrix formalism. At first we consider a closed V-type system and the density matrix equations that describe the system are derived under steady-state conditions. Later on, our density matrix analysis is extended to an open molecular system similar to that examined experimentally.

A closed three-level atomic system interacting with two near resonant fields is depicted in Figure 5a. The two excited levels |1> and |3> can radiatively decay to the ground state level |2> with decay rates W_{12} and W_{32}, respectively. The rate for internal radiative decay between levels |1> and |3> is denoted W_{13}, although this value is usually close to zero. In this V-shaped closed system, the transition |2> ↔ |1> is coupled to a weak radiation field (probe) of frequency ω_1 while the transition |2> ↔ |3> is coupled to a strong coupling field of frequency ω_2.

The unperturbed Hamiltonian $\hat{H}_o$ of the system is given by

$$\hat{H}_o = \sum_{i=1}^{3} \varepsilon_i \, | i >< i | \tag{1}$$

where the three discrete level energies have been arranged such that $\varepsilon_2 < \varepsilon_3 < \varepsilon_1$. The interaction Hamiltonian $\hat{H}_{\text{int}}(t)$ of the system is

$$\begin{aligned} \hat{H}_{\text{int}}(t) &= \hbar\Omega_1 (e^{-i\omega_1 t} + e^{i\omega_1 t})(| 1 >< 2 | + | 2 >< 1 |) \\ &+ \hbar\Omega_2 (e^{-i\omega_2 t} + e^{i\omega_2 t})(| 2 >< 3 | + | 3 >< 2 |) \end{aligned} \tag{2}$$

where we denote by Ω_1 and Ω_2 the Rabi frequencies of the probe and coupling fields, respectively, defined as $\Omega_1 = \frac{\mu_{12} E_1}{2\hbar}$ and $\Omega_2 = \frac{\mu_{32} E_2}{2\hbar}$, with μ_{ij} being the relevant transition dipole moment. Switching to the interaction picture, summation of the two contributions produces the total Hamiltonian $\hat{H}_I$ of the system, which after adaptation of the rotating-wave approximation is rewritten as:

$$\begin{aligned} \hat{H}_I &= \hbar\Omega_1 (| 1 >< 2 | + | 2 >< 1 |) + \hbar\Delta_1 \, | 1 >< 1 | \\ &+ \hbar\Omega_2 (| 2 >< 3 | + | 3 >< 2 |) + \hbar\Delta_2 \, | 3 >< 3 | \end{aligned} . \tag{3}$$

In the above expression we have defined the detunings of the applied fields assuming the molecules are not in motion and therefore do not experience inhomogeneous Doppler shifts:

$$\Delta_1 = \omega_{12} - \omega_1 \tag{4a}$$

for the detuning of the probe field, and

$$\Delta_2 = \omega_{32} - \omega_2 \tag{4b}$$

for the detuning of the coupling field. The detunings in eqs. 4a and 4b are in units of angular frequency, rad/s, while in the figures of the experimental scans and the simulations, the detunings are in Hz.

The evolution of the system is governed by the density matrix equations of motion, given by

$$\frac{d\rho_I}{dt} = -\frac{i}{\hbar}[H_I, \rho_I] + relaxation\ terms. \qquad (5)$$

However, our experimental system can be considered as open since the population leaving either of the two excited states |1> and |3> does not necessary end up in the ground state |2> but may also decay to many other lower levels. In our model, all lower states, other than |2>, to which decay from levels |1> and |3> is possible, are represented by level |4>. The levels |1> and |3> (rovibrational levels of the first excited electronic state $A^1\Sigma_u^+$ *(*v'*, J')* of the sodium dimer) can decay to any rovibrational level of the ground electronic state ($X^1\Sigma_g^+$) with *J" = J'*±1 (P and R branch) rotational quantum numbers in accordance with the electric dipole selection rules. The presence of extra decay channels from the upper levels |1> and |3> makes the molecular system "open" in comparison to a "closed" atomic system, where the levels |1> and |3> can only decay to |2>. Schematic comparison of the two V-type schemes is given in Figure 5.

In the experiment only continuous wave (CW) lasers were used, and thus a steady state approximation in Eq. (5) can be made ($d\rho_I/dt = 0$). By taking into account the specific decay processes, the individual components of Eq. (5) can be expressed as:

$$i\Omega_1(\rho_{12} - \rho_{21}) - W_1^t \rho_{11} = 0 \qquad (6.a)$$

$$i\Omega_1(\rho_{11}-\rho_{22})-d_1\rho_{12}+i\Omega_2\rho_{13}=0 \tag{6.b}$$

$$i\Omega_2\rho_{12}-d_2\rho_{13}-i\Omega_1\rho_{23}=0 \tag{6.c}$$

$$i\Omega_1(\rho_{11}-\rho_{22})+\tilde{d}_1\rho_{21}+i\Omega_2\rho_{31}=0 \tag{6.d}$$

$$-i\Omega_1(\rho_{12}-\rho_{21})+i\Omega_2(\rho_{23}-\rho_{32})+W_{12}\rho_{11}+W_{32}\rho_{33}-w_t\left(\rho_{22}-\rho_{22}{}^{e}\right)=0 \tag{6.e}$$

$$-i\Omega_1\rho_{13}+i\Omega_2(\rho_{22}-\rho_{33})-d_3\rho_{23}=0 \tag{6.f}$$

$$-i\Omega_2\rho_{21}-\tilde{d}_2\rho_{31}+i\Omega_1\rho_{32}=0 \tag{6.g}$$

$$i\Omega_1\rho_{31}-i\Omega_2(\rho_{22}-\rho_{33})-\tilde{d}_3\rho_{32}=0 \tag{6.h}$$

$$i\Omega_2(\rho_{23}-\rho_{32})+W_3^t\rho_{33}=0 \tag{6.i}$$

$$W_{14}\rho_{11}+W_{34}\rho_{33}-w_t\left(\rho_{44}-\rho_{44}{}^{e}\right)=0\,. \tag{6.j}$$

For simplicity in the notation we have introduced d_1, d_2, and d_3, defined as $d_1 \equiv i\Delta_1+\gamma_{12}^t$, $d_2 \equiv i\Delta_1-i\Delta_2+\gamma_{13}^t$, and $d_3 \equiv -i\Delta_2+\gamma_{23}^t$, and $\tilde{d}_i$ denotes the complex conjugate of d_i. In addition, we define $W_i^t \equiv W_i+w_t$ and $\gamma_{ij}^t \equiv \gamma_{ij}+w_t$, where w_t is the rate for transit relaxation, which takes into account the fact that molecules in all levels leave the interaction region by thermal motion and are replaced by other molecules from the bulk vapor that are statistically distributed over the ground state levels |2> and |4>. In particular, this is the primary mechanism for repopulating level |2> from level |4>. W_i indicates the natural decay rate of state |*i*>, while W_{ij} indicates the spontaneous emission rate from level *i* to *j*, and $\rho_{ii}{}^{e}$ is the population of level |*i*> at thermal equilibrium. γ_{ij}, is defined as the coherence dephasing rate between levels |*i*> and |*j*>, and is given by

$$\gamma_{ij} = \gamma_{ji} = \frac{1}{2}\sum_k \left(W_{ik} + W_{jk}\right) + \gamma_{ij}^{col} \quad . \tag{7}$$

γ_{ij}^{col} is the collisional dephasing rate. The system of Eqs (6), plus the population conservation equation

$$\rho_{11} + \rho_{22} + \rho_{33} + \rho_{44} = 1 \tag{8}$$

can be solved numerically by using matrix methods [31]. Note that the closed system equations can be recovered from Eqs. (6) by setting $W_{i4} = 0$.

b). Perturbation Theory Solution

Although the simulations have been performed with the full density matrix solution, the perturbation theory solution provides physical insight to the system. The exact analytical solution of the system of equations (6) is generally complicated. However, the probe laser is always much weaker (or at least weaker) than the coupling laser in the experiments. Therefore, a perturbative technique [32] that seeks a solution in the form of an expansion in powers of the probe laser Rabi frequency can be used, with the general form:

$$\rho_{ij} = \sum_{k=0}^{\infty} r_{ij}^{(k)} \Omega_1^k \ . \tag{9}$$

Depending on the value of Ω_1 and the desired level of accuracy for a particular ρ_{ij} a cutoff in the expansion can be made, and in the limiting case of negligibly small Ω_1 (very weak probe laser) compared to the other parameters of the system, the expansions for ρ_{ij} can be cut at the first nonzero terms. The coefficients $r_{ij}^{(k)}$ are found by combining (6) and (8) and solving the resulting equations for each power of Ω_1 . The properties of the V scheme excitation system in the experiments are revealed by the probe laser. To interpret and explain the experimental results we need expressions for ρ_{12} and ρ_{11} . The level |1> fluorescence signal in the experiments is a measure of the population of level |1>, which is represented in the model by ρ_{11} . From Eq. (6.a) we see that the diagonal matrix element ρ_{11} is directly proportional to the imaginary part of ρ_{12} . The first non vanishing terms for ρ_{12} and ρ_{11} are the $r_{12}^{(1)}$ and $r_{11}^{(2)}$ terms, respectively. Thus in the weak probe limit ($\Omega_1 \to 0$) for ρ_{12} and ρ_{11} we have

$$\rho_{12} = r_{12}^{(1)}\Omega_1 \tag{10}$$

$$\rho_{11} = r_{11}^{(2)}\Omega_1^2 \tag{11}$$

The explicit form of $r_{12}^{(1)}$ and $r_{11}^{(2)}$ can be obtained by incorporating Eq. (9) in the system (6) and solving the resulting equations for each order of Ω_1 . For $r_{12}^{(1)}$ we obtain

$$r_{12}{}^{(1)} = \frac{\Omega_2 r_{23}{}^{(0)} - i d_2 r_{22}{}^{(0)}}{d_1 d_2 + \Omega_2{}^2} \quad . \tag{12}$$

and using the relation

$$r_{11}^{(k+1)} = \frac{i}{W_1^t}\left(r_{12}^{(k)} - r_{21}^{(k)}\right) = -\frac{2}{W_1^t}\,\mathrm{Im}\left[r_{12}^{(k)}\right], \qquad k = 1,2,3,... \tag{13}$$

$r_{11}^{(2)}$ can easily be obtained

$$r_{11}{}^{(2)} = \frac{2}{W_1^t}\,\mathrm{Im}\left[\frac{i d_2 r_{22}{}^{(0)} - \Omega_2 r_{23}{}^{(0)}}{d_1 d_2 + \Omega_2{}^2}\right]. \tag{14}$$

In Eqs. (12) and (14) $r_{22}{}^{(0)}$ and $r_{23}{}^{(0)}$ are the zeroth order terms of ρ_{22} and ρ_{23}

$$r_{22}^{(0)} = \frac{W_3^t d_3 \widetilde{d}_3 + 2\gamma_{23}^t {\Omega_2}^2}{W_3^t d_3 \widetilde{d}_3 + 2\gamma_{23}^t \alpha {\Omega_2}^2} {\rho_{22}}^e, \tag{15}$$

$$r_{23}{}^{(0)} = \frac{i\Omega_2}{d_3} \frac{W_3^t d_3 \widetilde{d}_3}{W_3^t d_3 \widetilde{d}_3 + 2\gamma_{23}^t \alpha {\Omega_2}^2} {\rho_{22}}^e, \tag{16}$$

where $\alpha = \left(2 + \frac{W_{34}}{w_t} \right)$. Note that α is a measure of the openness of the system for a weak probe.

By combining Eqs. (11), (14), (15), and (16) we obtain an expression giving the explicit dependence of the population of level |1> on the parameters of the system, such as Ω_i, γ_{ij}, W_{ij}, and W_i, in the weak probe limit:

$$\rho_{11} = F(\Delta_2) \mathrm{Re}\left[\frac{(d_2 d_3 - \Omega_2^2)\widetilde{d}_3 W_3^t + d_2 {\Omega_2}^2 2\gamma_{23}^t}{d_1 d_2 + {\Omega_2}^2} \right] \Omega_1^2 \tag{17}$$

with

$$F(\Delta_2) = \frac{2}{W_1^t} \cdot \frac{{\rho_{22}}^e}{W_3^t (\Delta_2^2 + {\gamma_{23}^t}^2) + 2\Omega_2^2 \gamma_{23}^t \alpha} \quad . \tag{18}$$

The experimentally recorded intensity of the fluorescence signal as a function of the detuning of the probe laser (Δ_1) is directly proportional to the population of level |1> represented in the model by ρ_{11}. In general, Eq. (17) is a complicated expression in terms of Δ_1 and Δ_2. However, if we set $\Delta_2 = 0$, a series of manipulations allows the resonant structure of $\rho_{11}(\Delta_1)$ to be revealed [30]. Specifically, we obtain:

$$\rho_{11} = \gamma_{23}^t F(\Delta_2 = 0) \frac{(\Delta_1^2 - \gamma_{12}^t \gamma_{13}^t - {\Omega_2}^2)\Omega_2^2 W_3^t + (\gamma_{23}^t W_3^t + 2{\Omega_2}^2)(\gamma_{13}^t {\Omega_2}^2 + \gamma_{12}^t (\Delta_1^2 + {\gamma_{13}^t}^2))}{((\Delta_1 + \Delta_{1,+})^2 + \Gamma^2)((\Delta_1 + \Delta_{1,-})^2 + \Gamma^2)} \Omega_1^2 \tag{19}$$

where we have defined $\Gamma \equiv \frac{\gamma_{13}^{t} + \gamma_{12}^{t}}{2}$ and $\Delta_{1,\pm} \equiv \pm\frac{1}{2}\sqrt{4\Omega_2{}^2 - \left(\gamma_{13}^{t} - \gamma_{12}^{t}\right)^2}$. In this form we can see that $\rho_{11}(\Delta_1)$ has a minimum at $\Delta_1 = 0$ (where the numerator of Eq. (19) is minimized) and that the maxima of $\rho_{11}(\Delta_1)$ are found at $\Delta_1 = \Delta_{1,\pm}$ (minimizing the denominator). In the limit of a strong coupling field the maxima are given by $\Delta_{1,\pm} = \pm\Omega_2$, which represent the positions of the Autler-Townes doublet components, as expected.

c). Inclusion of the Doppler Effect and the Observed Fluorescence Signal

The experiments presented earlier were carried out in a heat pipe oven. Therefore, our theoretical model should account for the inhomogeneous Doppler broadening that is experienced by the molecular system. Due to the Doppler effect, the diatomic molecules in the heat-pipe "see" the optical laser fields with shifted frequencies. Thus, in the case of co-propagating fields, the laser field detunings of the Doppler broadened system will be given by

$$\delta_1(\upsilon_z) = \Delta_1 + \omega_1 \frac{\upsilon_z}{c} = \Delta_1 + k_1\upsilon_z \tag{20}$$

$$\delta_2(\upsilon_z) = \Delta_2 + \omega_2 \frac{\upsilon_z}{c} = \Delta_2 + k_2\upsilon_z \tag{21}$$

where k_1 and k_2 are the wavenumbers of the probe and coupling fields, respectively, Δ_1 and Δ_2 are the nominal detunings for stationary molecules defined by Eq. (4) and υ_z is the *z* component of velocity of the molecule.

On the other hand, when the two laser beams are in a counter-propagating geometry, the velocity dependent detunings $\delta_1(\upsilon_z)$ and $\delta_2(\upsilon_z)$ are expressed as

$$\delta_1(\upsilon_z) = \Delta_1 + \omega_1 \frac{\upsilon_z}{c} = \Delta_1 + k_1 \upsilon_z \tag{22}$$

$$\delta_2(\upsilon_z) = \Delta_2 - \omega_2 \frac{\upsilon_z}{c} = \Delta_2 - k_2 \upsilon_z \,. \tag{23}$$

Hence, the behavior of the system can be calculated by replacing Δ_1 and Δ_2 by $\delta_1(\upsilon_z)$ and $\delta_2(\upsilon_z)$, respectively, in all density matrix equations, and performing an average over the molecular velocity distribution [33].

The Doppler-broadened spectral lines can be represented in detail by a convolution of Lorentzian and Gaussian profiles, known as a Voigt profile [34]. The velocity distribution of the molecules is described by a Maxwellian distribution,

$$N(\upsilon_z) = \frac{N_o}{u_p \sqrt{\pi}} \exp\left(-\frac{\upsilon_z{}^2}{\upsilon_p{}^2} \right) \,, \tag{24}$$

where N_o is the molecular density and $\upsilon_p = \left(\frac{2kT}{m} \right)^{\frac{1}{2}}$ is the most probable velocity of a molecule. The contribution of all molecules with different velocity components along the axis of light propagation is obtained by integrating every density matrix element over the distribution $N(\upsilon_z)$. Thus,

$$\left\langle \rho_{ij} \right\rangle_{Doppler} = \int_{-\infty}^{\infty} \rho_{ij}(\upsilon_z) N(\upsilon_z) d\upsilon_z \quad . \tag{25}$$

An additional effect considered in our model is the spatial variation of the laser power density in the radial direction. Each of the molecules, interacting with the tightly focused laser beams, encounters a different laser power density depending on their location and consequently experiences a different Autler-Townes effect [35], leading to additional broadening of the spectral line. In this case, the theoretical absorption or fluorescence signal is obtained by performing an additional integration over the transverse laser beam profiles depending on the radial position *r* of the molecule with respect to the light propagation axis *z*. When the *r*-averaging over the beam profile is inserted into our fluorescence spectrum calculations, we note a slight change in the wings of the spectral line while the central part, where the dip appears, remains unaffected.

Each level with rotational angular momentum *J* in a particular electronic and vibrational state of a diatomic molecule is composed of 2*J*+1 discrete magnetic sub-levels M_J. The interaction of the optical field with the magnetic sub-levels depends on the type of transition it induces (P, Q or R) and whether it is linearly or circularly polarized. Then, the M_J-dependent Rabi frequency of a transition (v″, *J*″)→(v′, *J*′) is determined by a rotational strength factor *f* [36]

$$\Omega_{i,M}(r) = \frac{\mu_{el} |< \mathrm{v}'', \mathrm{v}' >| E_i}{\hbar} f \cdot \exp[-(r / w_i)^2], \qquad (26)$$

where E_i is the amplitude of the applied field, w_i is the beam waist spot size, μ_{el} is the electronic transition dipole moment, and $|< \mathrm{v}'', \mathrm{v}' >|$ is the square root of the Franck–Condon factor of the given transition.

A detailed discussion on the calculation of the transition dipole moment orientation factors *f*, for different types of molecular electronic transitions and field polarizations, is given by Spano [37]. Specifically, for the type of ${}^1\Sigma^+ \to {}^1\Sigma^+$ electronic transitions used in our experiment, the rotational strength factors *f* induced by a linearly polarized laser field are

$$f_R = \sqrt{\frac{1}{(2J+1)(2J+3)}}\sqrt{(J+1)^2 - {M_J}^2} \quad , \quad \text{for an R transition} \tag{27}$$

and

$$f_P = \sqrt{\frac{1}{(2J+1)(2J-1)}}\sqrt{J^2 - {M_J}^2} \qquad , \quad \text{for a P transition.} \tag{28}$$

Finally, after including in our analysis the Doppler-broadening, the variation of the laser power density over space, and the magnetic sub-level dependence, we obtain numerically the observed fluorescence signal (population of level |1>) from

$$\langle \rho_{11} \rangle_{M_J, r-average, Doppler} = \sum_{M_J} \int_0^{\infty} r dr \int_{-\infty}^{\infty} \rho_{11}(\upsilon_z, r) N(\upsilon_z) d\upsilon_z \ . \tag{29}$$

IV. Simulated Experimental Data and Discussion

The two-photon residual Doppler linewidth [2] for a three-level V-system is

$$\Delta \nu_D = \left| \overrightarrow{k_1} - \overrightarrow{k_2} \right| \mathrm{v_p} \ . \tag{30}$$

Obviously, if the two applied optical fields propagate along the same direction, the residual Doppler linewidth is minimized and the situation is similar to that occurring in an almost Doppler-free environment. In addition, by selecting both lasers with nearly equal wavelengths one can almost cancel the two-photon Doppler width. Under such a beam configuration an EIT dip can be observed in a closed V-type Doppler broadened system for relatively low coupling field Rabi frequency [2, 3, 38]. In contrast, when the two laser fields are in a counter-propagating configuration, the residual Doppler linewidth increases significantly creating unfavorable conditions for the observation of Autler-Townes splitting and EIT. The effect of minimizing the residual Doppler width on the probe laser lineshape in a closed three level V-scheme is depicted in Figure 6. Here we plot absorption signal $\mathrm{Im}\,\rho_{12}$, which is proportional to ρ_{11} according to Eq. 6.a. The numerical calculations indicate that the EIT realized in a closed system is strongly affected by the beam geometry of the applied fields. However, in an open molecular V-type system, EIT in combination with incoherent saturation effects can be physically observed even for residual Doppler linewidths greater than the induced Autler-Townes splitting. The difference in the absorption spectrum of the |2> → |1> transition for the same open molecular system explored by two laser fields in co- and counter-propagating geometries is shown in Figure 7. It is obvious that to separate EIT from saturation effects additional theoretical analysis is required as shown in the simulation of saturation effects below.

In all simulations, real experimental parameters were employed and the proper laser beam geometries were considered. It has been experimentally shown that the lifetimes of different ro-vibrational energy levels of the $A^1\Sigma_u^+$ electronic state in Na_2 are of the same order [39]. Thus, in our theoretical predictions the lifetimes W_1^{-1} and W_3^{-1} of levels |1> and |3>, respectively, were taken to be 12.23 ns [39]. In addition, the collisional dephasing rates for all levels were approximated as $\gamma_{ij}^{col} = 2\pi \times 5$ MHz.

The transient relaxation rate w_t corresponding to our experimental set-up was calculated according to several proposed models [40-42]. Our simulations were performed by employing a transit time broadening rate of $w_t/2\pi = 3$ MHz. The critical parameters in the model are the Rabi frequencies of the applied optical fields which have been estimated using Eq. (26). The Rabi frequency of the probe field was unchanged in both experimental arrangements being approximately equal to 10 MHz. In contrast, the Rabi frequency of the coupling field was different for the case of co- and counter-propagating beams because of slightly different focusing.

With the beams in a co-propagating configuration, we theoretically predict the population of the upper level |1> using the experimental parameters, and compare the simulated probe laser induced fluorescence lineshape with experimental data when the coupling laser field is on or near resonance (see Figure 8). In the two cases shown, a sharp dip in the fluorescence spectrum is predicted and observed. The agreement between the theoretical results and the experimentally observed spectra is very good. Thus, in experiments where the chosen beam geometry acts to reduce the residual Doppler line width, our model seems to describe the coherence effects quite accurately.

Next, we compare our numerical results with experimental data for the counter-propagating beam geometry. Two main modifications have been made to the coupling field which influence the EIT contrast in comparison to the co-propagating case: the laser intensity is 275 mW and the spot size is 986 μm, resulting in a Rabi frequency of approximately 240 MHz for the strong |2> → |3> transition. After taking into account the above changes we perform a numerical simulation and notice further, as shown in Figure 9, that the experimental results compare well with the model results.

Since it is difficult to design the above experiments for beams with different geometry ensuring the same experimental parameters (e.g. laser intensities, beam profiles) or conditions (e.g. spatial overlap between probe and coupling fields) it is convenient to compare the two systems via theoretical calculations.

Simulations to isolate the Saturation Effects

As described in [2], there are a couple of simultaneously occurring mechanisms in a V-type system which cannot be easily distinguished. The two relevant ones for our case are EIT and saturation by the coupling field. The density matrix equations should be able to reproduce all these various contributions since they deal with both population and coherence effects. In order to distinguish between effects due to coherent versus incoherent processes (EIT vs. saturation) and to determine which process(es) is (are) responsible for the dips observed in our fluorescence data, we study the equations of motion Eqs. (6.a – 6.j).

In a two-level, one–laser excitation scheme, the single laser pump term corresponding to a ρ_{12} coherence, can be written in terms of $\rho_{11} - \rho_{22}$ (i.e., if there is only one laser coupling to the particular levels, then the density matrix equations reduce to rate equations and the pump term reduces to a difference between stimulated emission and absorption rates). If we now consider the V–type scheme with two lasers present, then the coherences become more complicated because of the ρ_{13} term in addition to the direct laser ρ_{12} and ρ_{32} terms. However, if we set $\rho_{13} = 0$, then we can effectively turn off all of the coherence effects involving the interplay of the two laser fields (i.e., with $\rho_{13} = 0$, then ρ_{12} and ρ_{32} can be written simply in terms of the population differences, $\rho_{11} - \rho_{22}$ and $\rho_{33} - \rho_{22}$, respectively. Therefore, by setting the coherence ρ_{13} to zero, and then solving the density matrix equations of motion, Eqs. (6.a-6.j), for the open system, we can study the effects of saturation by itself and distinguish them from those caused by EIT.

From (6.b) and (6.d), under the condition that $\rho_{13} = 0$, we obtain an equation for the ρ_{12} coherence:

$$\rho_{12} = \tilde{\rho}_{21} = \frac{i\Omega_1}{d_1}\left(\rho_{11} - \rho_{22}\right) \; . \tag{31}$$

After substituting Eq. (31) into (6.a) we obtain an expression relating the ground state (level |2>) and level |1> populations

$$\rho_{22} = F_{12}\rho_{11} \, , \tag{32}$$

where the coefficient of proportionality F_{ij} is defined as

$$F_{ij}\left(W^t_{2i-1}, \gamma^t_{ij}, \Delta_i, \Omega_i\right) = \frac{W^t_{2i-1}\left(\Delta_i^2 + {\gamma^t_{ij}}^2\right) + 2\Omega_i^2\gamma^t_{ij}}{2\Omega_i^2\gamma^t_{ij}} \tag{33}$$

Similarly, from (6.f) and (6.h) the coherences ρ_{23} and ρ_{32} are given by

$$\rho_{23} = \tilde{\rho}_{32} = \frac{i\Omega_2}{d_3}\left(\rho_{22} - \rho_{33}\right), \tag{34}$$

and using (6.i), this leads to

$$\rho_{33} = \frac{1}{F_{23}}\rho_{22} \tag{35}$$

Substituting the expressions for the various level populations (Eqs. 32, 35, and 6.j) into the equation for population conservation given by Eq. (8), we arrive at the final expression for the excited state level |1> population, which corresponds to the fluorescence signal detected in our experiment:

$$\rho_{11} = \frac{{\rho_{22}}^e}{1 + \frac{W_{14}}{w_t} + F_{12} + \left(1 + \frac{W_{34}}{w_t}\right)\frac{F_{12}}{F_{23}}} \, . \tag{36}$$

After integrating Eq. 36 over the Doppler profile and performing a summation for all magnetic sublevels M_J, as given by Eq. 29, we can study the effects of saturation alone on the state |1> fluorescence under different experimental conditions.

Figure 10 shows comparative calculations for the population of state |1> for the two different beam geometries in the presence of both coherent and incoherent effects ($\rho_{13} \neq 0$) and in the case of saturation only ($\rho_{13} = 0$). As we can see, in the co-propagating case, saturation is responsible for only part of the depth of the dip in the fluorescence spectrum, indicating that a significant fraction of the depth of the dip seen in Figure 10a, and in the experiment, is due to the coherent effect of EIT. At the same time, when the coupling and probe beams are in the counter-propagating configuration, there is very little difference in the fluorescence line shape between the cases when two-laser coherences are included and when only pumping and stimulated emission (i.e. saturation) effects are present (see Figure 10b). This leads us to conclude that the dip observed in the experimental signal is primarily due to saturation alone in the counter-propagating case within the accuracy of the present measurements.

We repeated the simulations for the case of a closed system, achieved by closing the decay channels to state |4>, e.g. by setting the decay rates W_{34} and W_{14} to zero (Figure 11). Our calculations show that saturation is responsible for a dip of modest depth in either of the propagation geometries, while EIT dramatically increases the depth in the co-propagating case and fills in the dip in the counter-propagating case.

Figure 12 shows probe laser lineshapes calculated for different coupling laser intensities (i.e., different values of the coupling laser Rabi frequency Ω_2) for both co- and counter-propagating geometries and with both $\rho_{13} \neq 0$ (saturation effects plus EIT) and $\rho_{13} = 0$ (saturation effects only). Here, the population of state 1 (ρ_{11}) is plotted in the same relative units for all curves. So it can be seen that in all cases, increasing coupling laser intensity results in lower populations in level 1. In the co-propagating case with all coherence effects included (Fig. 12.a) we see that the dip is almost 100% over a wide range of coupling laser Rabi frequencies, and that the width of the dip (and also the separation of the peaks) increases monotonically with increasing Rabi frequency. This is the case where the two-photon Doppler linewidth is small, and we see that EIT in combination with saturation causes two peaks split apart by the AT effect, and almost complete transparency at line center due to the combined effects of EIT and AT. The case of counter-propagating lasers with all coherence effects included (Fig. 12.c) shows very different behavior. Here the dip is narrow and fairly deep at lower coupling laser Rabi frequency, but as the Rabi frequency is increased, the dip becomes shallower (as a percentage of the peak amplitude) and wider until it disappears altogether at $\Omega_2/2\pi$ = 1000 MHz (i.e., comparable to the Doppler broadening). The splitting of the peaks at first increases with increasing Rabi frequency, but the overall linewidth decreases at high Rabi frequency when the dip disappears. Figs. 12.b and 12.d show the cases where the ρ_{13} coherence has been set to zero. First of all, we note that in this case, there is no difference between the co- and counter-propagating geometries. Here, the dip is due to saturation alone, and it can be seen that the depth of the dip (as a percentage of the peak amplitude) first grows with increasing Rabi frequency, but then the dip broadens and becomes less deep as the Rabi frequency continues to increase. Thus the effects of EIT can be clearly seen in the co-propagating case, but are much more difficult to distinguish in the counter-propagating case.

V. Conclusions

We report here the experimental observation of EIT in Doppler broadened sodium dimer gas using a V-type excitation scheme. The experiment is performed with two different arrangements for the propagation directions of the coupling and probe beams (e.g. co- or counter-propagating). In our theoretical model we employ the density matrix formalism, as well as perturbative methods for obtaining the probe field absorption profile. Simulation of the experimental data under real experimental conditions shows excellent agreement with the predictions derived from the basic theory. Our fluorescent intensity measurements show that in the co-propagating configuration the EIT plus saturation window depth is about 95%, while under similar conditions in the counter-propagating geometry we observed 40-45% reduction in the fluorescence signal around line center. Using theoretical calculations we show that in the co-propagating case a significant fraction of the depth of the dip is due to the coherent effect of EIT and when the coupling and probe beams are in counter-propagating configuration, the dip is mostly due to saturation effects alone.

Acknowledgements

We acknowledge valuable early discussions with Prof. Lorenzo M. Narducci of Drexel University and more recently discussions with Prof. Jianbing Qi of Penn State Berks Campus. This work was supported by NSF grants PHY 0555608, PHY 0855502, and PHY 0968898.

Figures

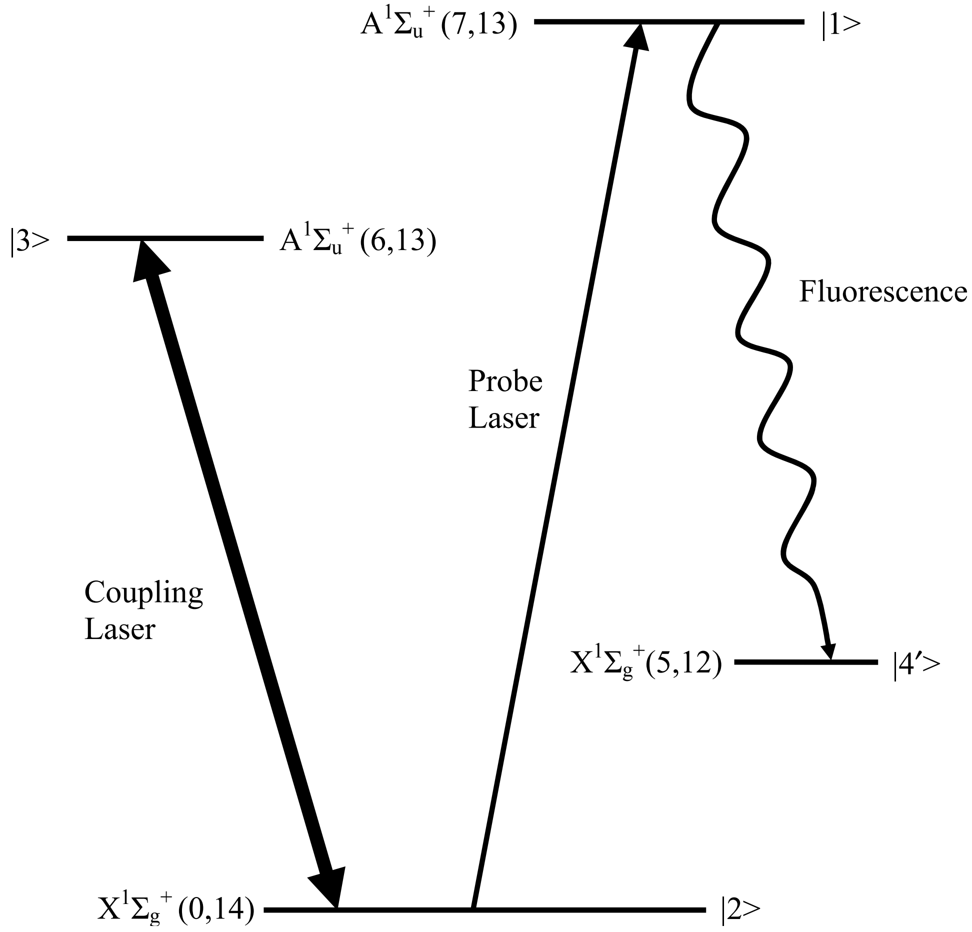

Figure 1 The V-type excitation scheme for the Na_2 system. The laser frequency corresponding to the $X^1\Sigma_g^+$(v″=0, J″=14) → $A^1\Sigma_u^+$(v′=6, J′=13) coupling transition is 15315.7695 cm^{-1} and that for the probe transition $X^1\Sigma_g^+$(v″=0, J″=14) → $A^1\Sigma_u^+$(v′=7, J′=13) is 15448.1451 cm^{-1}. The monochromator was set to 681.4 nm to monitor the fluorescence from the upper level $A^1\Sigma_u^+$(v′=7, J′=13) to the ground state level $X^1\Sigma_g^+$(v″=5, J″=12). The Frank-Condon factors of the probe and coupling field transitions are 0.113 and 0.101, respectively.

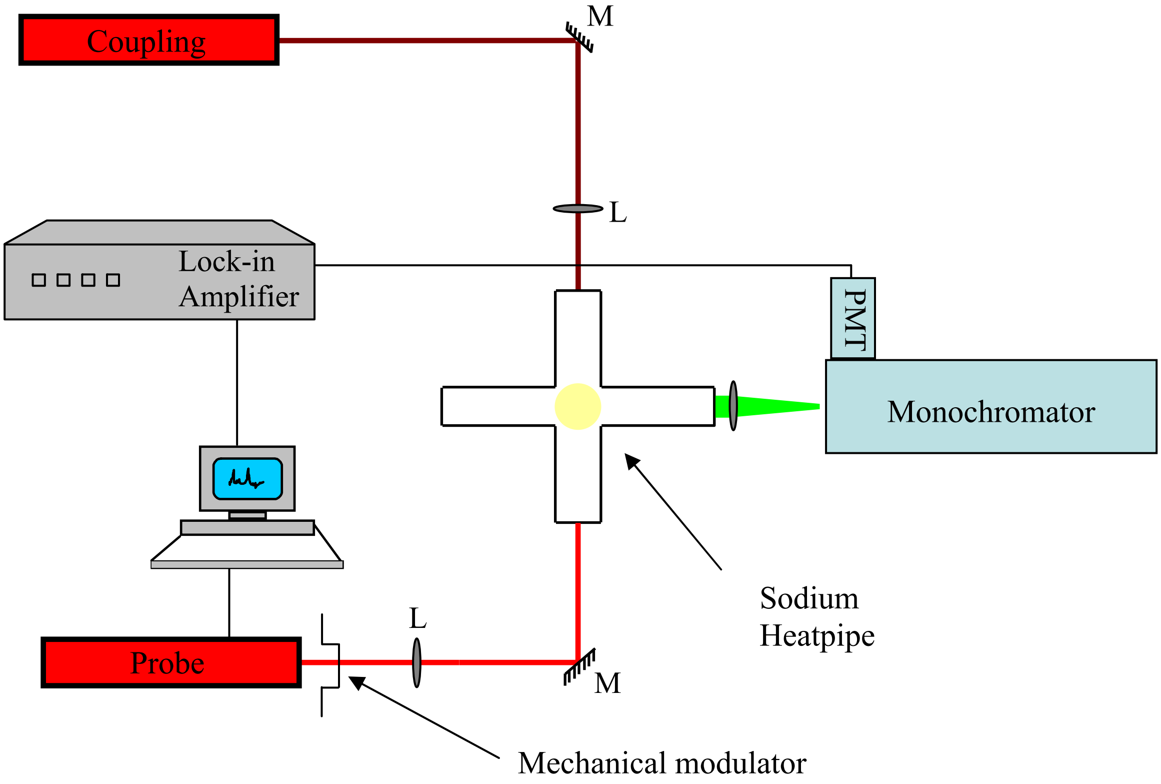

Figure 2 Experimental setup for the V-scheme EIT experiment. The coupling and probe laser beams propagate in opposite directions. A mechanical chopper is used to modulate the probe field while neutral density filters allow the attenuation of the each laser field. M = mirror, L = lens.

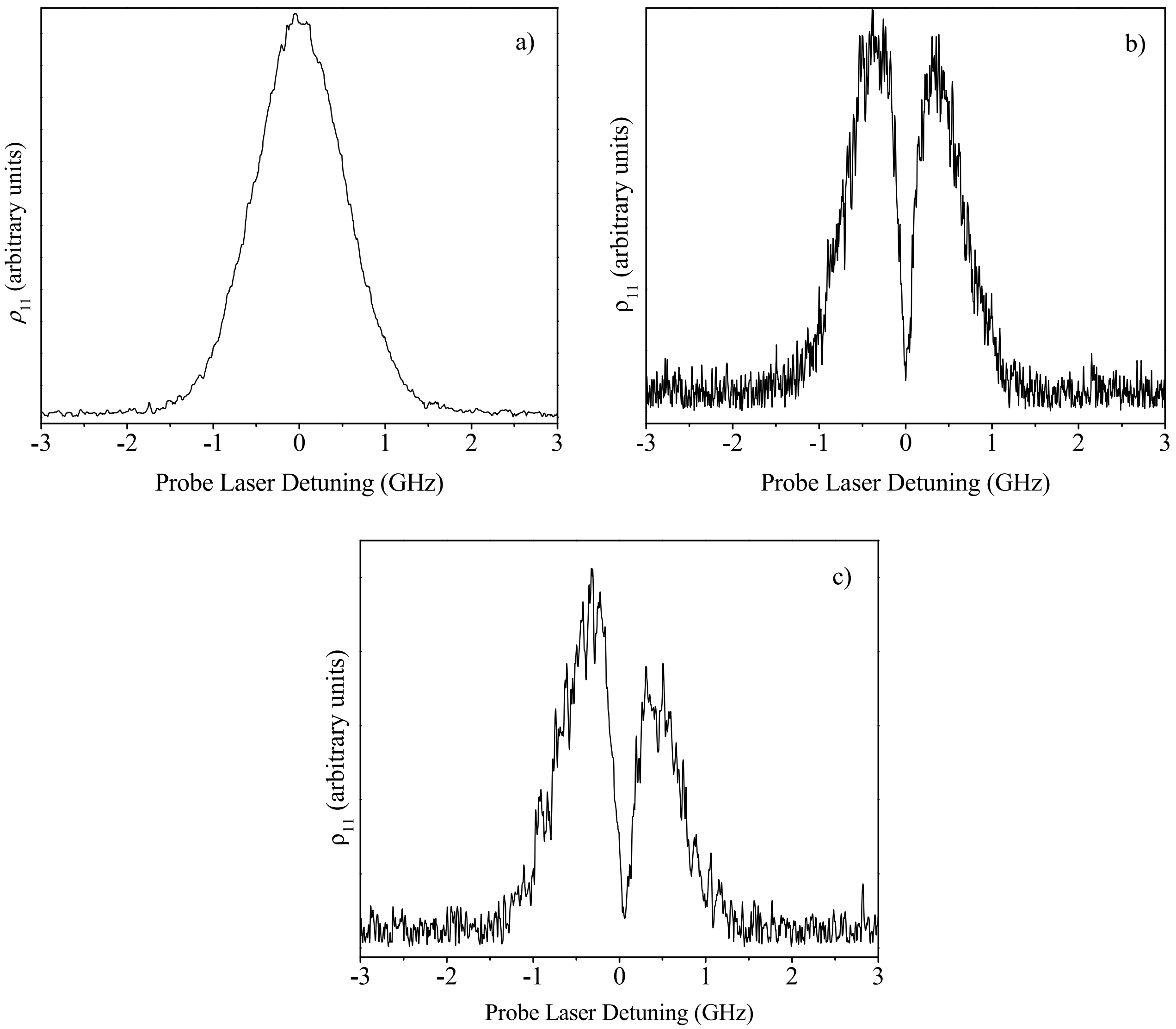

Figure 3 Experimental spectra for Na$_2$ V-system probe laser scans in the co-propagating geometry. a) with the coupling field turned off. b) with the coupling field on, and the frequency of the coupling laser is set to line center of the transition. c) The coupling field is detuned by ~60 MHz. The coupling laser power is 265-270 mW and the probe laser power is less than 1 mW.

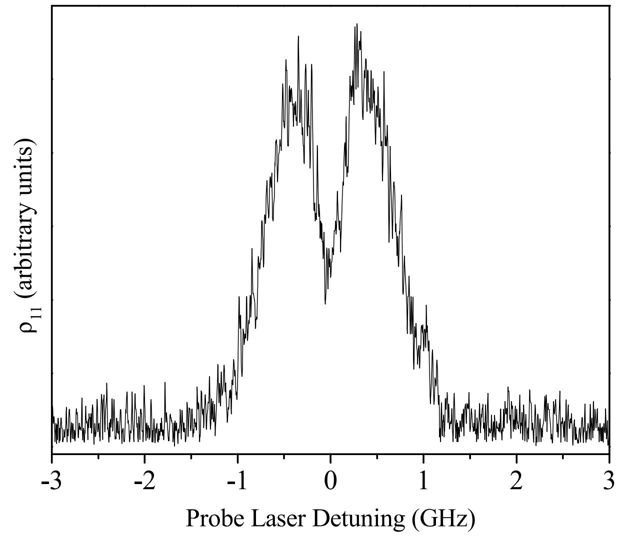

Figure 4 Experimental spectra for counter-propagating laser beams. While the coupling field is on resonance the probe field is scanned and fluorescence from level |1> (which is proportional to the level |1> population) is recorded. The power of the coupling and probe lasers were 350 mW and 120 μW, respectively.

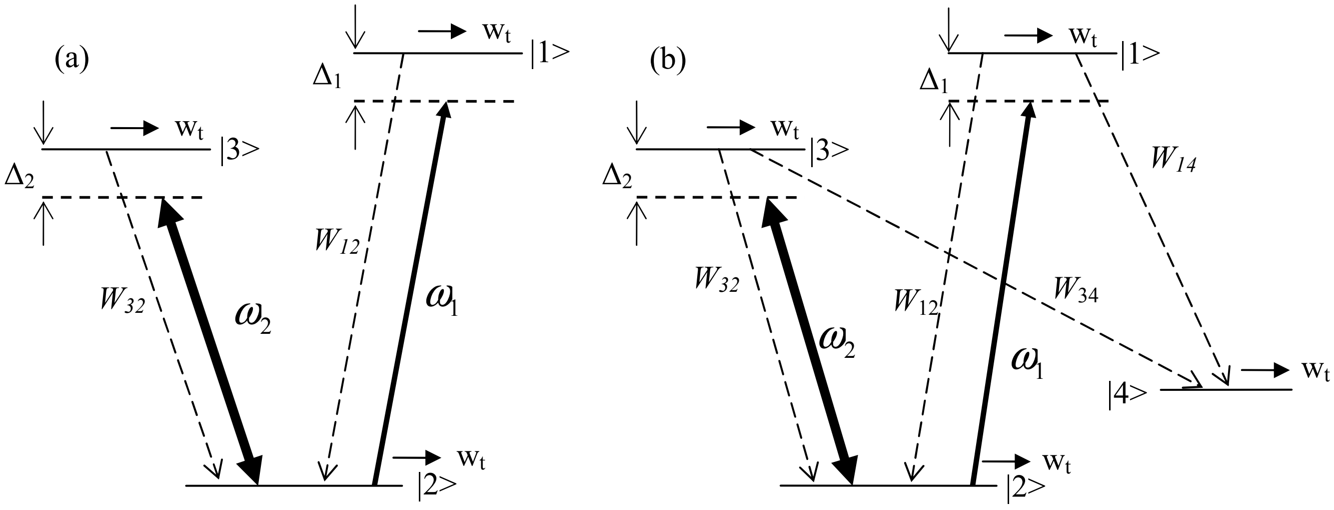

Figure 5 Pumping and relaxation processes for (a) closed and (b) open 3-level V-type systems. A weak probe field with frequency ω_1 and detuning Δ_1 couples the |2> → |1> transition. Levels |2> and |3> are coupled by a strong coupling field with frequency ω_2 and detuning Δ_2. In (b), molecules occupying the excited energy levels |1> and |3> can follow various relaxation pathways and decay to many ground state levels besides level |2>. In our model all these levels are represented by level |4>. W_{ij} indicates the spontaneous emission rate of level |i> to level |j> while the natural decay rate of level |i> is denoted W_i. The decay rates of the ground state levels |2> and |4> are negligible. The Rabi frequencies of the probe and coupling fields are Ω_1 and Ω_2, respectively, and w_t is the transient relaxation rate of the molecules entering and leaving the interaction region. Due to selection rules in our system there is no decay from |1> to |3>.

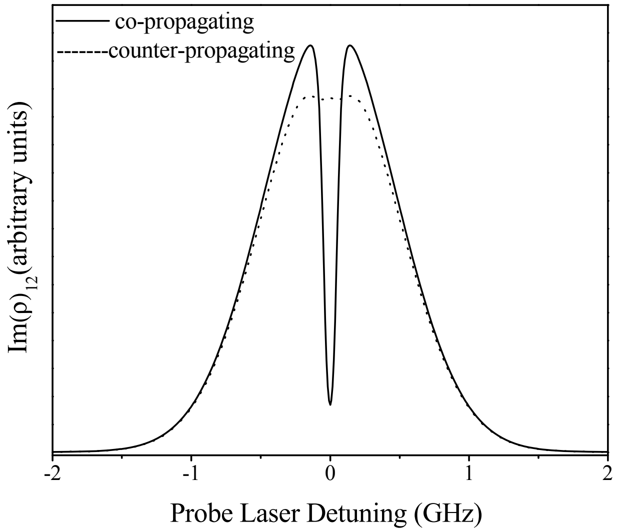

Figure 6 Three-level closed atomic V-type system. The theoretical absorption profile of the probe laser is given for co-propagating (solid line) and counter-propagating (dashed line) beam geometries. The Rabi frequencies for the coupling and probe fields are taken to be 250 MHz and 10 MHz, respectively. In the counter-propagating case, a much stronger field is needed in order to observe the Autler-Townes splitting. The full Doppler width in both simulations is 1.2 GHz.

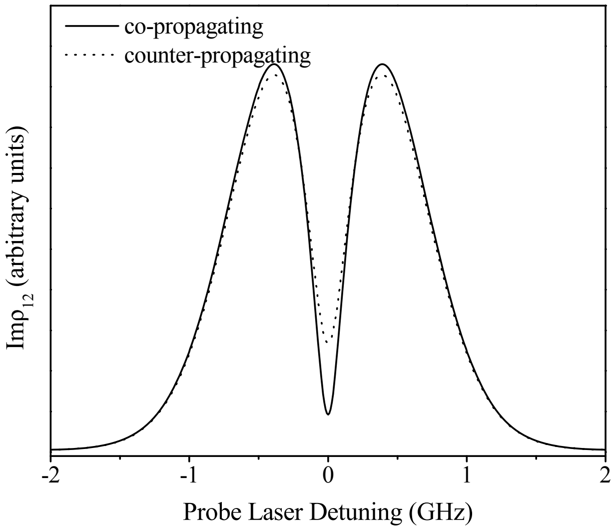

Figure 7 Three-level open molecular V-type system. The absorption profile as a function of the probe laser detuning is given for co-propagating (solid line) and counter-propagating (dashed line) beam geometries. The applied fields are the same as in Figure 6.

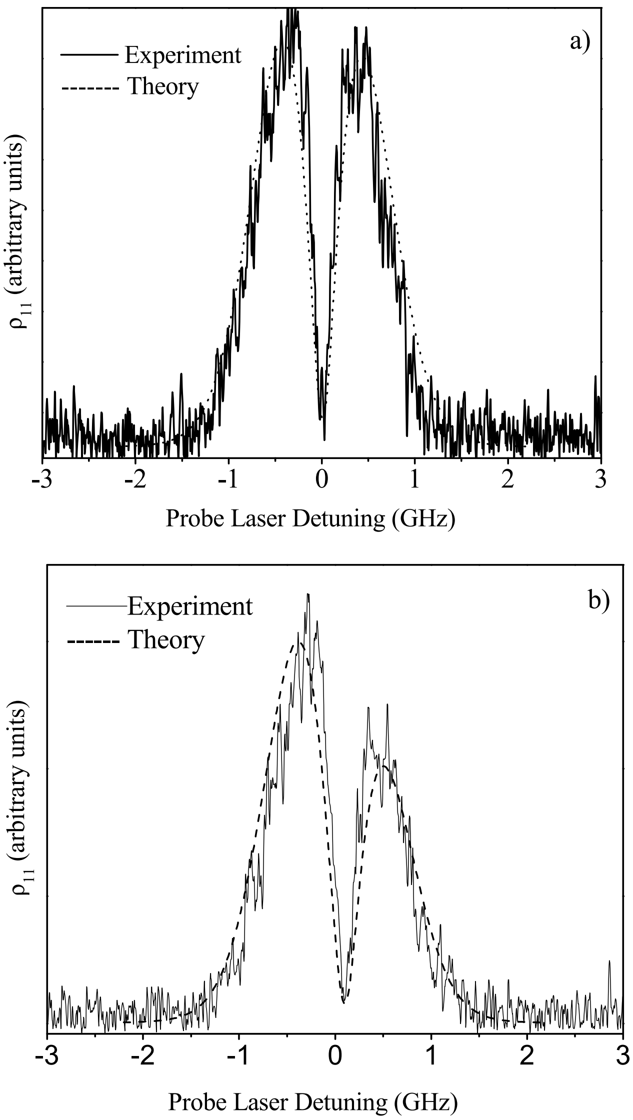

Figure 8 Experimental (solid line) and simulated (dashed line) data for co-propagating beams. By inserting the real experimental parameters in our density matrix equations we simulate the experimental data when (a) the coupling field is on resonance with Ω_2=220 MHz and (b) the coupling field is detuned 100 MHz with Ω_2=190 MHz. The Rabi frequency of the probe laser was 10 MHz in both cases.

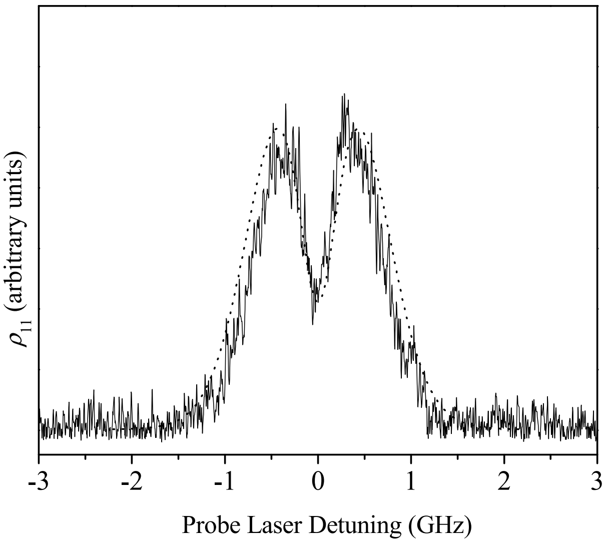

Figure 9 Experimental (solid line) and simulated (dashed line) data for counter-propagating beams. The coupling and probe lasers propagate in the opposite directions with powers of 275 mW and 120 μW, respectively. The openness of the molecular system is responsible for the observation of a reduction in the population of level |1> (or reduction of the probe laser absorption) at line center.

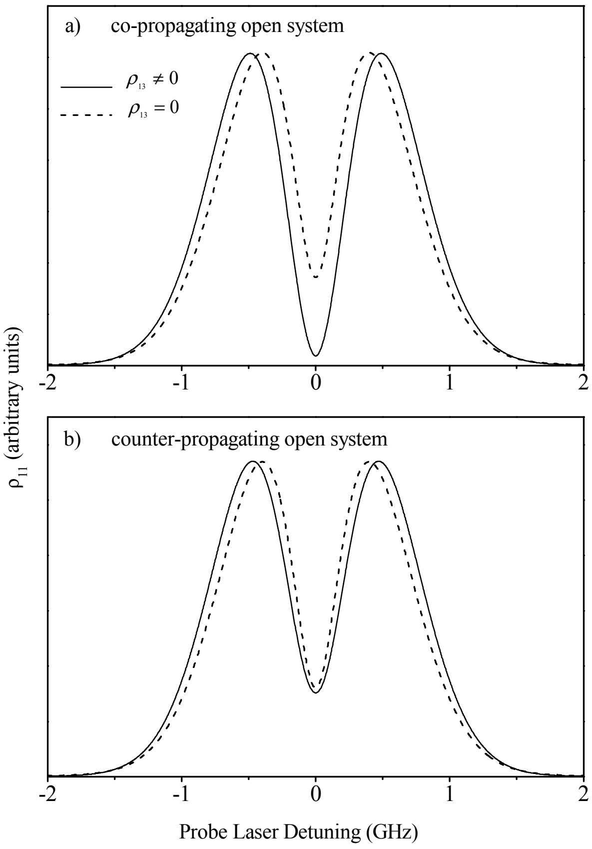

Figure 10 Comparison between (a) co- and (b) counter- propagating fluorescence signals for the cases of $\rho_{13} \neq 0$ (solid line) and $\rho_{13} = 0$ (dashed line) in an open 3-level V-type system. The calculation of the population of level |1> is carried out using parameters close to the experimental conditions: $\Omega_1 / 2\pi = 10MHz,\ \Omega_2 / 2\pi = 220MHz,\ \gamma_{ij}^{col} / 2\pi = 0.79MHz$.

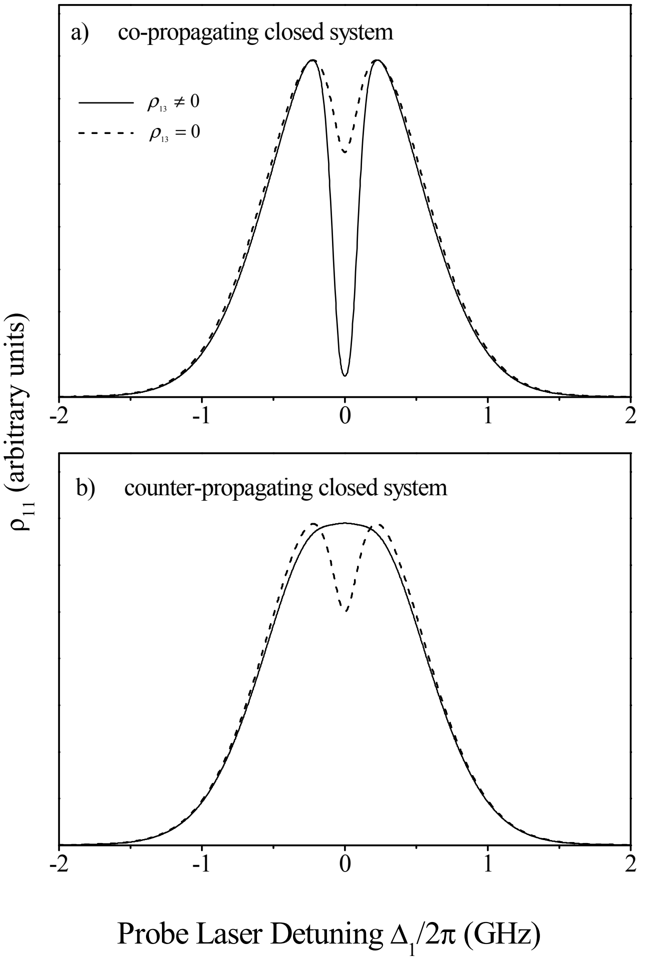

Figure 11 Comparison between (a) co- and (b) counter-propagating fluorescence signals for the cases of $\rho_{13} \neq 0$ (solid line) and $\rho_{13} = 0$ (dashed line) in a closed 3-level V-type system. The calculation of the population of level |1> is carried out using parameters close to the experimental conditions: $\Omega_1 / 2\pi = 10 MHz$, $\Omega_2 / 2\pi = 220 MHz, \gamma_{ij}^{col} / 2\pi = 0.79 MHz$

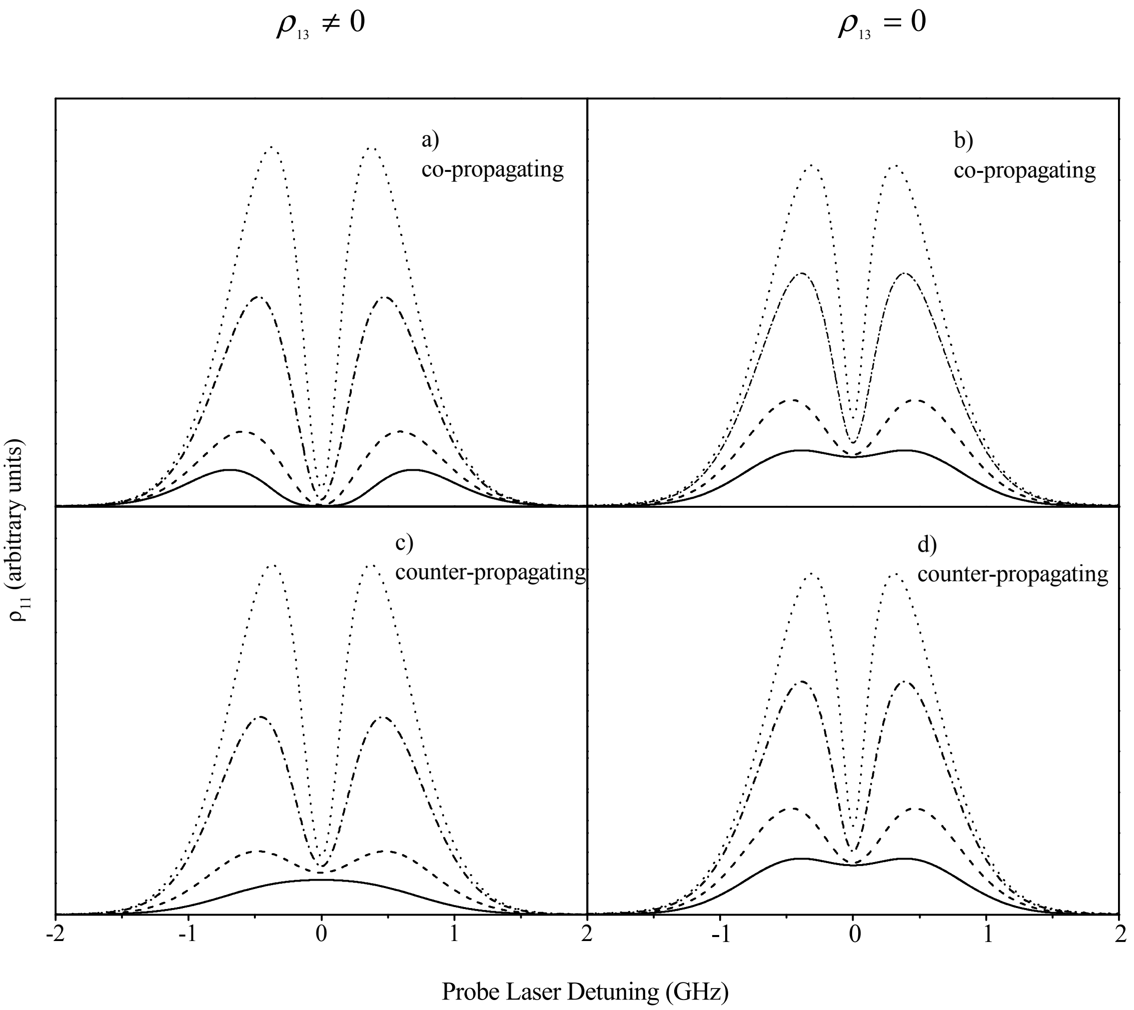

Figure 12 Power study of the co- and counter-propagating fluorescence signals for the cases of $\rho_{13} \neq 0$ [(a) and (c)] and $\rho_{13} = 0$ [(b) and (d)] in an open 3-level V-type system. The calculation of the population of level |1> is carried out using parameters close to the experimental conditions: $\Omega_1 / 2\pi = 10MHz$, $\gamma_{ij}^{col} / 2\pi = 0.79MHz$. The coupling laser Rabi frequency is

varied: $\Omega_2 / 2\pi = 100, 200, 500, 1000 MHz$ for the dotted, dot-dashed, dashed and solid curves, respectively.

References

1. J. E. Field, K. H. Hahn, and S. E. Harris, Phys. Rev. Lett. **67**, 3062 (1991).
2. D. J. Fulton, S. Shepherd, R. R. Moseley, B. D. Sinclair, and M. H. Dunn, Physical Review A **52**, 2302 (1995).
3. Y. Q. Li and M. Xiao, Physical Review A **51**, R2703 (1995).
4. Y. F. Zhu and T. N. Wasserlauf, Physical Review A **54**, 3653 (1996).
5. S. Baluschev, N. Leinfellner, E. A. Korsunsky, and L. Windholz, European Physical Journal D **2**, 5 (1998).
6. K. J. Boller, A. Imamoglu, and S. E. Harris, Physical Review Letters **66**, 2593 (1991).
7. G. R. Welch, G. G. Padmabandu, E. S. Fry, M. D. Lukin, D. E. Nikonov, F. Sander, M. O. Scully, A. Weis, and F. K. Tittel, Foundations of Physics **28**, 621 (1998).
8. J. P. Marangos, Journal of Modern Optics **45**, 471 (1998).
9. J. Qi, F. C. Spano, T. Kirova, A. Lazoudis, J. Magnes, L. Li, L. M. Narducci, R. W. Field, and A. M. Lyyra, Physical Review Letters **88**, 173003 (2002).
10. A. Lazoudis, T. Kirova, E. H. Ahmed, L. Li, J. Qi, and A. M. Lyyra, Physical Review A **82** (2010).

11. L. Li, P. Qi, A. Lazoudis, E. Ahmed, and A. M. Lyyra, Chemical Physics Letters **403**, 262 (2005).

12. A. Lazoudis, E. H. Ahmed, L. Li, T. Kirova, P. Qi, A. Hansson, J. Magnes, and A. M. Lyyra, Physical Review A **78**, 043405 (2008).

13. S. Ghosh, J. E. Sharping, D. G. Ouzounov, and A. L. Gaeta, Physical Review Letters **94**, 093902 (2005).

14. F. Benabid and P. J. Roberts, Journal of Modern Optics **58**, 87 (2011).

15. P. S. Light, F. Benabid, G. J. Pearce, F. Couny, and D. M. Bird, Applied Physics Letters **94**, 141103 (2009).

16. H. Li, H. Chen, M. A. Gubin, Y. V. Rostovtsev, V. A. Sautenkov, and M. O. Scully, Laser Physics **20**, 1725 (2010).

17. E. Ahmed, A. Hansson, P. Qi, T. Kirova, A. Lazoudis, S. Kotochigova, A. M. Lyyra, L. Li, J. Qi, and S. Magnier, Journal of Chemical Physics **124**, 084308 (2006).

18. E. H. Ahmed, P. Qi, B. Beser, J. Bai, R. W. Field, J. P. Huennekens, and A. M. Lyyra, Physical Review A **77**, 053414 (2008).

19. S. J. Sweeney, E. H. Ahmed, P. Qi, T. Kirova, A. M. Lyyra, and J. Huennekens, Journal of Chemical Physics **129**, 154303 (2008).

20. O. Salihoglu, P. Qi, E. H. Ahmed, S. Kotochigova, S. Magnier, and A. M. Lyyra, Journal of Chemical Physics **129**, 174301 (2008).

21. E. H. Ahmed, P. Qi, and A. M. Lyyra, Physical Review A **79** (2009).

22. C. H. Townes and A. L. Schawlow, *Microwave Spectroscopy,* (McGraw-Hill publishing Company Ltd., London, 1955).

23. S. Shepherd, D. J. Fulton, and M. H. Dunn, Physical Review A **54**, 5394 (1996).

24. C. R. Vidal and J. Cooper, Journal of Applied Physics **40**, 3370 (1969).

25. A. N. Nesmeyanov, *Vapor Pressure of the Chemical Elements* (Elsevier, 1963).

26. P. Kusch and M. M. Hessel, J. Chem. Phys. **68**, 2591 (1978).

27. O. Babaky and K. Hussein, Can. J. Phys. **67**, 9112 (1989).

28. P. Qi, J. Bai, E. Ahmed, A. M. Lyyra, S. Kotochigova, A. J. Ross, C. Effantin, P. Zalicki, J. Vigué, G. Chawla, R. W. Field, T.-J. Whang, W. C. Stwalley, H. Knöckel, E. Tiemann, J. Shang, L. Li, and T. Bergeman, J. Chem. Phys. **127**, 044301 (2007).

29. K. Ichimura, K. Yamamoto, and N. Gemma, Physical Review A **58**, 4116 (1998).

30. E. Ahmed and A. M. Lyyra, Physical Review A **76**, 053407 (2007).

31. A. S. Manka, H. M. Doss, L. M. Narducci, P. Ru, and G.-L. Oppo, Physical Review A **43**, 3748 (1991).

32. R. W. Boyd, *Nonlinear Optics* (Academic Press, New York, 1992).

33. S. N. Sandhya and K. K. Sharma, Physical Review A **55**, 2155 (1997).

34. W. Demtröder, *Laser Spectroscopy* (Springer-Verlag, Berlin Heidelberg, 1996).

35. B. Girard, G. O. Sitz, R. N. Zare, N. Billy, and J. Vigue, Journal of Chemical Physics **97**, 26 (1992).

36. Y. B. Band and P. S. Julienne, Journal of Chemical Physics **97**, 9107 (1992).

37. F. C. Spano, Journal of Chemical Physics **114**, 276 (2001).

38. J. Gea-Banacloche, Y. Li, S. Jin, and M. Xiao, Physical Review A **51**, 576 (1995).

39. G. Baumgartner, H. Kornmeier, and W. Preuss, Chemical Physics Letters **107**, 13 (1984).

40. J. E. Thomas and W. W. Quivers, Physical Review A **22**, 2115 (1980).

41. E. V. Baklanov, B. Y. Dubetskii, V. M. Semibalamut, and E. A. Titov, Kvantovaya Elektronika **2**, 2518 (1975).

42. J. L. Hall, *Lectures in Theoretical Physics* (Gordon Brendi and Co., New York, 1970).